

Strong-Field Theory of Attosecond Tunneling Microscopy

Boyang Ma^{1,2,3} and Michael Krüger^{1,2,3,*}

¹*Department of Physics, Technion—Israel Institute of Technology, Haifa 32000, Israel*

²*Solid State Institute, Technion—Israel Institute of Technology, Haifa 32000, Israel*

³*The Helen Diller Quantum Center, Technion—Israel Institute of Technology, Haifa 32000, Israel*

(Dated: October 1, 2024)

Attosecond observations of coherent electron dynamics in molecules and nanostructures can be achieved by combining conventional scanning tunneling microscopy (STM) with ultrashort femtosecond laser pulses. While experimental studies in the sub-cycle regime are underway, a robust strong-field theory description has remained elusive. Here we devise a model based on the strong-field approximation. Valid in all regimes, it provides a surprising analogy to the standard model of STM. We also show that the intuitive three-step model of attosecond science directly emerges from our model and describe the optimal conditions for attosecond STM experiments.

Scanning tunneling microscopy (STM) enables atomic-scale imaging of electronic states of surfaces and molecules [1–3], but lacks attosecond and femtosecond time resolution which characterizes electron dynamics in a wide range of systems, for example molecular charge migration [4, 5]. A straightforward approach to achieve time resolution in an STM is inducing and controlling tunneling currents between an atomically sharp metallic probe tip and a sample using phase-controlled ultrashort intense laser pulses. It is well known that the electric field waveform of such pulses can coherently control electron tunneling on the attosecond time scale in gases [6, 7] and bulk solids [8, 9] and at metallic surfaces [10], metallic nanotips [11–14] and nanodevices [15–19]. However, initial femtosecond STM experiments (see, e.g., [20–24]) faced numerous experimental challenges and only recently, attosecond control of tunneling currents was achieved in an STM [25]. In the latter work, the authors were able to observe the transition from the multiphoton regime to the strong-field regime where tunneling occurs. Here, shifting the carrier-envelope phase (CEP) of 6 fs near-infrared pulses assisted by a DC voltage enabled strong modulations of the tunneling current and the generation of attosecond bursts of tunneling electrons between the tip and a metallic sample. The basic mechanism behind the modulation is the strong sensitivity of tunneling to the instantaneous optical field, allowing for unipolar attosecond bursts of tunneling electrons inside an STM junction. This is very intriguing because it allows injecting or extracting electrons from a sample on the attosecond scale fully controlled by the laser field waveform alone, as shown already in the THz regime for the picosecond scale [26].

Existing strong-field theory models for ultrafast STM or, more generally, for ultrafast tunneling currents in nano-scale metal-insulator-metal (MIM) junctions are either analytical models, such as simple Fowler-Nordheim tunneling models [15, 17], a strong-field model for the tip emission only without the barrier [25] or a quasi-classical imaginary time method calculation [27], or *ab-initio* models, such as a numerical integration of the time-

dependent Schrödinger equation (TDSE) [25] or time-dependent density functional theory (TDDFT) simulations [17, 28, 29]. These models describe either partial aspects of the physics, such as the tunneling process, or provide exact results which are challenging to interpret. In this work, we introduce an intuitive and complete strong-field model for ultrafast laser-driven STM which provides deep insight into the underlying physical mechanisms. Applying the strong-field approximation (SFA) [30–32] to our problem, we find the intriguing three-step picture [33, 34] which beautifully describes the hallmark recollision effects of attosecond science, high-harmonic generation (HHG, [8, 35]), high-order above-threshold ionization (ATI, [36]) and photoemission (ATP, [11]), as well as non-sequential double ionization [37]. We identify an energy cutoff law, which is markedly different from the former effects, and describe the optimal conditions for performing attosecond tunneling experiments in an STM.

The ultrafast STM can be described as a static MIM junction illuminated by a near-infrared (NIR) femtosecond laser pulse (see Fig. 1(a) and (b)). We assume that the laser field is screened perfectly inside the tip and sample and is only present in the vacuum gap. When the laser turns on, the time-varying laser electric field drives electrons inside the junction, generating a laser-induced tunneling (LIT) current. Even though the STM is limited by the electronic response time, the time-integrated LIT current can be measured and recorded by the STM. Under the laser interaction, currents inside the STM can flow from the tip to the sample and vice versa. They can be thought of as independent current flows and can be modeled in the same way but with the opposite sign of the electric field (see Supplemental Material [38]). Therefore, for simplicity, we only focus on the current flow from the tip to the sample. Furthermore, the extremely sharp nanotip and the sample can generate a near-field in the gap, localizing the LIT current only at the tip apex [25]. Therefore, despite its simplicity, a one-dimensional treatment promises accurate calculations [25, 39, 40]. We define a spatial coordinate x and a junction width d . The tip-vacuum boundary is located at $x = 0$ (see Fig. 1(b)).

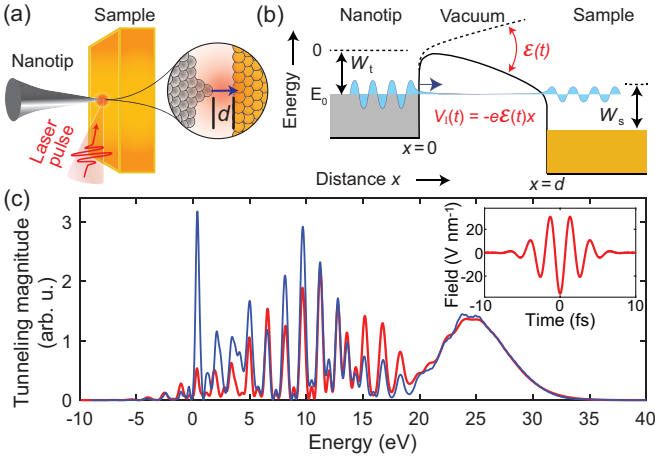


Figure 1. Strong-field theory for ultrafast STM. (a) A schematic of the ultrafast STM. (b) One-dimensional potential model of the laser-driven STM junction (W_t : tip work function, W_s : sample work function, \mathcal{E} : laser electric field). (c) The tunneling electron spectrum calculated by the TDSE (red) and our SFA theory (blue) following Eq. 3. Here, $d = 1$ nm, the pulse duration of the laser is 6 fs (full width at half maximum, see inset for the field waveform) and the field amplitude F is 35 V nm^{-1} . The material for tip and sample is gold ($W_t = W_s = 5 \text{ eV}$), the tip electron is initially at the Fermi energy $E_0 = -W_t = -5 \text{ eV}$. Static fields are absent.

In this letter, we study the time-integrated LIT current by analyzing the tunneling amplitude after the interaction (see Supplemental Material for detailed derivations [38]).

In the conventional STM, the tunneling amplitude can be described using Bardeen's tunneling theory [46], the standard theory approach for STM [47]. By defining the eigenfunction of the tip as Ψ_t and the eigenfunction of the sample at energy state E as ψ_E , the static tunneling current from tip to sample is proportional to the absolute square of Bardeen's tunneling matrix element C_{stat} , which is given by

$$C_{\text{stat}} = \frac{\hbar^2}{2m} \left[\Psi_t(x) \frac{\partial}{\partial x} \psi_E^*(x) - \psi_E^*(x) \frac{\partial}{\partial x} \Psi_t(x) \right]_{x=d}. \quad (1)$$

Here \hbar is the reduced Planck constant and m the electron mass. The superscript star represents the complex conjugate. In Bardeen's theory, the wave functions are assumed to be orthogonal to each other. The term in the brackets is evaluated at the boundary $x = d$, hence only the information of the wave functions at the vacuum-sample boundary is required while explicit information about the barrier potential remains absent. Despite its simplicity, Bardeen's tunneling theory enables quantitative modeling of STM (see Ref. [47] for details).

In the ultrafast STM, we need to solve a time-dependent problem involving a strong laser field to obtain the LIT current. Here we formulate the LIT amplitude

M_E in a form similar to C_{stat} (Eq. 1), which is given by

$$M_E = \frac{i\hbar}{2m} \int_{-\infty}^{\infty} \left[\Psi_{\text{Is}}(x, t) \frac{\partial}{\partial x} \psi^*(x, t) - \psi^*(x, t) \frac{\partial}{\partial x} \Psi_{\text{Is}}(x, t) \right]_{x=0}^{x=d} dt. \quad (2)$$

We have obtained M_E from expansions of the Dyson equation of the time-dependent Schrödinger equation [31, 48] (see the Supplemental Material for the complete derivation [38]). $\Psi_{\text{Is}}(x, t)$ is the time-propagated wave function driven by the laser, which is generated from $|\Psi_0\rangle$ inside the gap, where $|\Psi_0\rangle$ is the initial state of the system with an electron at the Fermi energy E_0 of the tip. The subscript "Is" represents the interaction with the static and time-dependent potentials (see Supplemental Material [38]). $\psi^*(x, t) = \langle \psi_E | \chi_s U(\infty, t) | x \rangle$ is nothing else than the complex conjugate of the wave function in the sample region propagated to a specific time. Here, we denote the full time evolution operator of the system as $U(t_2, t_1)$, with $t_2 > t_1$, and define χ_s to be 1 for $x \geq d$ and 0 elsewhere, which is an operator to select only the wave function in the sample region. The notation $[\dots]_{x=0}^{x=d}$ at the end of Eq. 2 stands for the subtraction of the term inside the brackets evaluated at $x = 0$ from the term evaluated at $x = d$.

The main difference to the Bardeen's expression is the fact that, in M_E , the matrix element is now time-dependent, requiring a time integration. We also note that Eq. 2 also includes the tip-vacuum boundary at $x = 0$. $\Psi_{\text{Is}}(x, t)$, which is driven back and forth in the laser field, can scatter at the tip boundary at $x = 0$, leading to a rescattering effect [11]. The LIT amplitude depends on the total flux through the junction boundaries, which is a direct result of the flux continuity (see Supplemental Material [38]). We find excellent agreement between solutions of Eq. 2 and a numerical solution of the full TDSE using the Crank-Nicolson scheme [11, 49] (see Supplemental Material [38]).

The presence of the time-dependent wave functions $\psi^*(x, t)$ and $\Psi_{\text{Is}}(x, t)$ in Eq. 2 are hindering us from studying the tunneling dynamics in a strong ultrashort laser field analytically. We therefore apply the SFA, which treats the laser-driven (continuum) electron as a free particle moving in the laser field (Volkov wave), neglecting any influence of the field-free potential [30–32]. In our specific case, we use two assumptions to apply the SFA. First, we neglect the effect of the image charge potential in the vacuum junction. The image charge is induced when an electron is present inside the junction, causing an attractive force towards the surfaces [50]. However, for laser field strengths on the order 10 V nm^{-1} and higher, this force is negligible compared to the force exerted by the laser field. Second, we ignore reflections of the wavefunction from the tip boundary $x = 0$ where the field-free potential has a high step. Such reflections have

been observed at nanotips and are known as rescattering. Here an electron is emitted from the tip, but returns to the tip surface after about 3/4 of an optical cycle and undergoes elastic scattering [11, 51]. However, the contribution from rescattering to the total current in those experiments is weak. Moreover, in strong fields on the order 10 V nm^{-1} and higher, most electrons cross the tiny STM junction in less than an optical half-cycle, hence the electron does not quiver and rescattering cannot take place [17]. In addition to these two assumptions, we also treat the sample region as an isolated system so that the wave function component which has been transmitted to the sample region evolves freely. This is justified by the fact that the electric field is strongly screened and hence there is no time-dependent force present in the sample region. Therefore, we replace $\psi^*(x, t)$ and $\Psi_{\text{Is}}(x, t)$ in Eq. 2 with the eigenfunction $\psi_E^*(x, t)$ and a superposition of Volkov wavefunctions $\Psi_V(x, t)$, respectively, and obtain the SFA expression

$$M_{E,\text{SFA}} = \frac{i\hbar}{2m} \int_{-\infty}^{\infty} \left[\Psi_V(x, t) \frac{\partial}{\partial x} \psi_E^*(x, t) - \psi_E^*(x, t) \frac{\partial}{\partial x} \Psi_V(x, t) \right]_{x=d} dt. \quad (3)$$

The laser field inside the junction excites the initial wave function from its ground state to a laser-driven Volkov continuum state and moves the excited wave function to the sample region, where this transport finishes by projection on the energy eigenstates of the sample. Figure 1(c) shows a comparison between Eq. 3 and a numerical integration of the TDSE (see Supplemental Material [38] for details of the TDSE). We assume a peak field of 35 V nm^{-1} for a 6-fs laser pulse at a central wavelength of 830 nm. The width of the STM junction between a gold nanotip and a gold sample is chosen as $d = 1 \text{ nm}$. We obtain excellent agreement between our strong-field model and the TDSE result.

Figure 2 shows the total LIT current vs field strength, revealing the different regimes of ultrafast STM depending on F and d . We also show the Keldysh parameter $\gamma = (\omega\sqrt{2m|E_0|})/(|e|F)$ [52]. TDSE calculation (Fig. 2(a)) and our strong-field model (Fig. 2(b)) are in good agreement. At $\gamma \gg 1$, the current scales linearly with intensity for $d \leq 1 \text{ nm}$. Here, a single photon is absorbed and static tunneling enables a transmission of the thus excited electron to the sample region (Fig. 2(c)). At increasing field strengths, but still at $\gamma > 1$, a transition to multiphoton excitation take place. Electrons that have absorbed more than one photon are either transmitted through static tunneling or over-barrier propagation (Fig. 2(d)). Notably, for a very thin barrier of 0.2 nm this transition to multiphoton excitation does not take place because the static tunneling remains extremely efficient. These phenomena have already been studied theoretically and experimentally based on weak perturbation

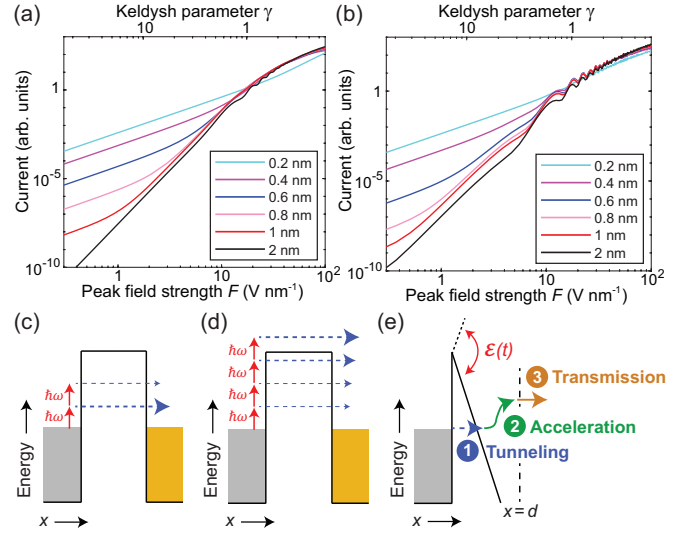


Figure 2. Regimes of ultrafast STM. (a) Double-logarithmic plot of LIT current vs. light peak field strength F and Keldysh parameter γ for different barrier widths d . The calculation is based on a numerical integration of the time-dependent Schrödinger equation for 6-fs pulses at 830 nm wavelength and a gold nanotip and sample. (b) The same plot calculated with the strong-field theory model (Eq. 3). (c) Weak-field regime with dominating one-photon excitation and subsequent static tunneling. (d) Multiphoton regime with subsequent static tunneling or over-barrier emission. (e) Field-driven tunneling regime with three steps – laser-driven tunneling, acceleration and transmission to the sample region.

methods [53, 54]. At $\gamma \sim 1$, we find the transition to the tunneling regime, in great similarity to nanotip photoemission, for instance [11, 14, 49, 55–58]. The curves for all barrier widths start to merge here because the laser field completely dominates the process and static tunneling does not have much of a role anymore for $\gamma < 1$. We note that our strong-field model magnifies the channel-closing effect with its strong oscillations around $\gamma = 1$, which should be only strong for large barrier widths according to the TDSE results.

Writing Eq. 3 more explicitly, we find a more intuitive SFA expression for the tunneling amplitude,

$$M_{E,\text{SFA}} = \int_{-\infty}^{\infty} \int_{-\infty}^{t_2} \sqrt{\frac{i}{8\pi m \hbar^3 (t_2 - t_1)}} \eta(t_2) \xi(t_1) \times \exp\left(\frac{i}{\hbar} S(t_2, t_1)\right) dt_1 dt_2, \quad (4)$$

with the semi-classical action

$$S(t_2, t_1) = Et_2 + \frac{\tilde{p}^2}{2m} (t_2 - t_1) - \int_{t_1}^{t_2} \frac{e^2 A^2(\tau)}{2m} d\tau + |E_0|t_1, \quad (5)$$

where e is the (negative) electron charge, $\tilde{p} =$

$(\int_{t_1}^{t_2} eA(\tau) d\tau + md)/(t_2 - t_1)$ is the canonical momentum and $A(t)$ is the vector potential of the light field which has a relation to the electric field $\mathcal{E}(t) = -\partial A(t)/\partial t$. The prefactors $\xi(t_1)$ and $\eta(t_2)$ describe normalization factors and transition matrix elements at times t_1 and t_2 (see Supplemental Material [38]). The time integrals in Eq. 4 and 5 can be analyzed using the saddle point method [30, 48, 49, 59]. We obtain the saddle point equations

$$\frac{[\tilde{p}_s - eA(t_{1s})]^2}{2m} = -|E_0|, \quad (6)$$

$$\int_{t_{1s}}^{t_{2s}} \frac{[\tilde{p}_s - eA(\tau)]}{m} d\tau = d, \quad (7)$$

$$\frac{[\tilde{p}_s - eA(t_{2s})]^2}{2m} = E, \quad (8)$$

where \tilde{p}_s is an effective canonical momentum which is conserved in the homogeneous electric field, and t_{1s} and t_{2s} are the saddle points of emission time and arrival time, respectively.

The above three saddle point equations give us a direct semi-classical scenario of the electron transport in ultrafast STM within the three-step trajectory picture, illustrated in Fig. 2(e): (1) emission by tunneling into the vacuum gap (Eq. 6), (2) acceleration by laser field across the gap (Eq. 7), and (3) transmission into the sample region (Eq. 8). The first saddle point equation enforces energy conservation at the emission time t_{1s} . The initial energy is negative, which leads to complex values for t_{1s} , t_{2s} and \tilde{p}_s . The imaginary part of the emission time is due to the classically forbidden dynamics under the barrier and can be interpreted as tunneling time [30, 60]. The second equation describes the displacement of the quasi-free electron accelerated by a homogeneous electric field. The electron starts moving at the emission time t_{1s} , but unlike the hallmark three-step recollision processes of attosecond science, we find in Eq. 7 that the electron does not return to the boundary $x = 0$, hence there is no recollision with the parent matter. Instead, it moves to the second boundary $x = d$. The last saddle point equation represents the energy conservation at the final time t_{2s} as the electron is transmitted into the sample region with a final energy E .

The saddle point equations can also be used to derive the classical cutoff energy. For a continuous wave light field, we obtain a law for cutoff energy of the form $E_{\text{cutoff}} = |e|(F_0 + F)d + E_0$, where F_0 is the static field that is usually present in an STM (see Supplemental Material [38]). Indeed, the TDSE simulations in Fig. 3(a) show that the tunneling spectrum beyond the classical cutoff is strongly attenuated. Our result stands in contrast to the cutoff laws of gas-phase HHG, ATI and ATP which depend on the ponderomotive energy which in turn is dependent on intensity and frequency. For ultrafast

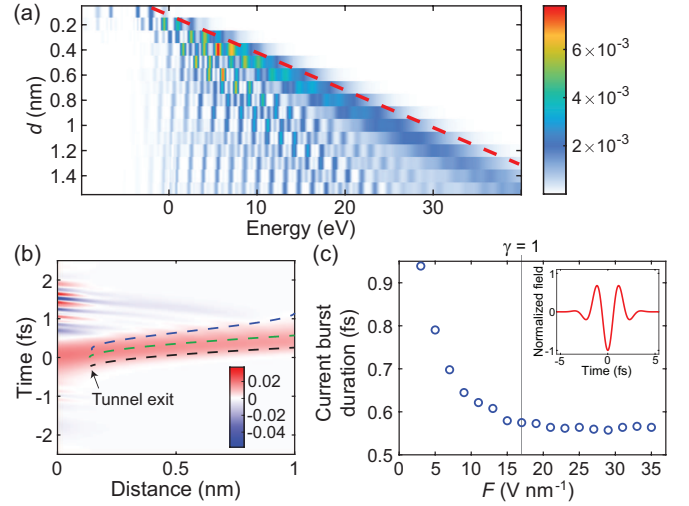


Figure 3. Cutoff and attosecond transport. (a) Spectrum of the tunneling electron as a function of d for the same parameters as Fig. 1(c) calculated with the TDSE. The red curve indicates the cutoff law derived from the saddle point equations. (b) Color plot of local currents as a function of space and time for $d = 1$ nm, $F = 35$ V nm $^{-1}$ and a 3-fs single-cycle laser pulse. From top to bottom, three curves show selected electron trajectories derived from the saddle-point equations for final energies of ~ 0 eV, 15 eV and 30 eV (cutoff), respectively. The laser field peaks at $t = 0$ fs. (c) Duration of the current burst as a function of F . Inset: Field wave form in (b) and (c).

STM, the decisive quantities are the total electric field $F_0 + F$ and the barrier width d , but there is no dependence on the frequency ω . The thin junction of the STM ensures that the transport finishes in a short time without any quiver motion, in analogy to near-field acceleration at nanotips [61, 62] and nanojunctions [17]. Figure 3(b) shows the local current density as a function of space and time inside a 3-fs light pulse at 35 V nm $^{-1}$ ($\gamma \sim 0.5$). Indeed, a single burst is generated at the central field crest at $t = 0$ and travels to the sample on the attosecond time scale. The dynamics of the burst correspond well with electron trajectories calculated using the saddle point equations (see Supplemental Material [38] for calculation details). Attosecond currents can be transported to the sample region within less than a femtosecond. The duration of the laser-driven tunneling burst is strongly connected to the Keldysh parameter (see Fig. 3(c)). As we increase the field strength and move from the multiphoton regime to the non-adiabatic tunneling regime [63], the duration decreases until it saturates at $\gamma \sim 1$ to a value of ~ 560 as where tunneling occurs adiabatically. This suggests that attosecond experiments can also be carried out in the non-adiabatic tunneling regime ($1 \lesssim \gamma \lesssim 4$) where the energy spread of the tunneling electron wavepacket is more limited. A sufficiently short CEP-stable laser can break the symmetry between the two directions of current flow between tip and sample, inducing current

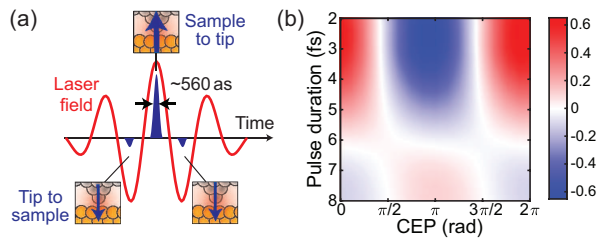


Figure 4. Symmetry breaking of tunneling solely by the laser field waveform. (a) Illustration of current rectification by a sub-two-cycle laser pulse. (b) Dependence of the total tunneling current and its sign on the carrier-envelope phase (CEP) for different pulse durations ($F = 17 \text{ V nm}^{-1}$, $\gamma \sim 1$ and $d = 1 \text{ nm}$). Strongly unipolar current bursts are found for 4 fs duration and shorter.

rectification controlled by the CEP (see Fig. 4(a) for an illustration). For instance, this ability may enable the extraction of an electron from a molecular sample driven by a CEP-stable pump pulse, followed by the injection of an electron into the remaining hole by a probe pulse with inverted CEP, opening up spatio-temporal imaging of ultrafast charge migration [5]. Such an experiment is challenging because it requires near-single-cycle pulses in order to achieve strong symmetry breaking solely by the laser field in the absence of a static field (see Fig. 4(b) and Supplemental Material [38]). However, experimental progress in single-cycle laser development and CEP-controlled currents in nano-junctions [15, 17] suggest that such symmetry breaking can be implemented also in an ultrafast STM.

In conclusion, we have introduced a strong-field theory for attosecond electron transport in ultrafast STM and other MIM junctions. Obtaining good agreement with an exact solution of the TDSE, we shed light on the transport mechanisms and the underlying temporal and spectral dynamics. We find the three-step picture at the heart of the tunneling regime of ultrafast STM. Possessing a strong versatility like other strong-field theories in attosecond science, our theory can be extended to include different materials, the density of states of sample and tip, the static field, image charge potential effects and the optical near-field enhancement inside the vacuum gap. We expect that our work will open the door to a rich interplay between theory and experiment at the extreme frontiers of spatio-temporal microscopy. Ultrafast pump-probe STM with phase-controlled current bursts will enable triggering and probing ultrafast charge dynamics in molecules, nanostructures and defect states, where a pump-probe delay-dependent, spatially localized current signal reveals charge oscillations on the femtosecond and attosecond time scales.

The authors acknowledge Zhaopin Chen and Yiming Pan for insightful discussions. This project has received funding from the European Union's Horizon 2020 research and innovation program under grant agreement

No 853393-ERC-ATTIDA and from the Israel Science Foundation under grant agreement No 1504/20. We also acknowledge the Helen Diller Quantum Center at the Technion for partial financial support.

* Corresponding author: krueger@technion.ac.il

- [1] G. Binnig, H. Rohrer, C. Gerber, and E. Weibel, Tunneling through a controllable vacuum gap, *Appl. Phys. Lett.* **40**, 178 (1982).
- [2] G. Binnig, H. Rohrer, C. Gerber, and E. Weibel, Surface studies by scanning tunneling microscopy, *Phys. Rev. Lett.* **49**, 57 (1982).
- [3] J. Repp, G. Meyer, S. M. Stojković, A. Gourdon, and C. Joachim, Molecules on insulating films: Scanning-tunneling microscopy imaging of individual molecular orbitals, *Phys. Rev. Lett.* **94**, 026803 (2005).
- [4] F. Lépine, M. Y. Ivanov, and M. J. J. Vrakking, Attosecond molecular dynamics: fact or fiction?, *Nat. Photon.* **8**, 195 (2014).
- [5] F. Calegari, G. Sansone, S. Stagira, C. Vozzi, and M. Nisoli, Advances in attosecond science, *J. Phys. B: At. Mol. Opt. Phys.* **49**, 062001 (2016).
- [6] M. Uiberacker, T. Uphues, M. Schultze, A. J. Verhoeef, V. Yakovlev, M. F. Kling, J. Rauschenberger, N. M. Kabachnik, H. Schroder, M. Lezius, K. L. Kompa, H. G. Muller, M. J. J. Vrakking, S. Hendel, U. Kleineberg, U. Heinzmann, M. Drescher, and F. Krausz, Attosecond real-time observation of electron tunnelling in atoms, *Nature* **446**, 627 (2007).
- [7] D. Shafrir, H. Soifer, B. D. Bruner, M. Dagan, Y. Mairesse, S. Patchkovskii, M. Y. Ivanov, O. Smirnova, and N. Dudovich, Resolving the time when an electron exits a tunnelling barrier, *Nature* **485**, 343 (2012).
- [8] G. Vampa, C. R. McDonald, G. Orlando, P. B. Corkum, and T. Brabec, Semiclassical analysis of high harmonic generation in bulk crystals, *Phys. Rev. B* **91**, 064302 (2015).
- [9] Y. S. You, M. Wu, Y. Yin, A. Chew, X. Ren, S. Gholam-Mirzaei, D. A. Browne, M. Chini, Z. Chang, K. J. Schafer, M. B. Gaarde, and S. Ghimire, Laser waveform control of extreme ultraviolet high harmonics from solids, *Opt. Lett.* **42**, 1816 (2017).
- [10] A. Apolonski, P. Dombi, G. G. Paulus, M. Kakehata, R. Holzwarth, T. Udem, C. Lemell, K. Torizuka, J. Burgdörfer, T. W. Hänsch, and F. Krausz, Observation of light-phase-sensitive photoemission from a metal, *Phys. Rev. Lett.* **92**, 073902 (2004).
- [11] M. Krüger, M. Schenk, and P. Hommelhoff, Attosecond control of electrons emitted from a nanoscale metal tip, *Nature* **475**, 78 (2011).
- [12] B. Piglosiewicz, S. Schmidt, D. J. Park, J. Vogelsang, P. Gross, C. Manzoni, P. Farinello, G. Cerullo, and C. Lienau, Carrier-envelope phase effects on the strong-field photoemission of electrons from metallic nanostructures, *Nat. Photon.* **8**, 37 (2014).
- [13] H. Y. Kim, M. Garg, S. Mandal, L. Seiffert, T. Fennel, and E. Goulielmakis, Attosecond field emission, *Nature* **613**, 662 (2023).
- [14] P. Dienstbier, L. Seiffert, T. Paschen, A. Liehl, A. Leitenstorfer, T. Fennel, and P. Hommelhoff, Tracing at-

- tosecond electron emission from a nanometric metal tip, *Nature* **616**, 702 (2023).
- [15] T. Rybka, M. Ludwig, M. F. Schmalz, V. Knittel, D. Brida, and A. Leitenstorfer, Sub-cycle optical phase control of nanotunnelling in the single-electron regime, *Nat. Photon.* **10**, 667 (2016).
 - [16] W. P. Putnam, R. G. Hobbs, P. D. Keathley, K. K. Berggren, and F. X. Kärtner, Optical-field-controlled photoemission from plasmonic nanoparticles, *Nat. Phys.* **13**, 335 (2017).
 - [17] M. Ludwig, G. Aguirregabiria, F. Ritzkowski, T. Rybka, D. C. Marinica, J. Aizpurua, A. G. Borisov, A. Leitenstorfer, and D. Brida, Sub-femtosecond electron transport in a nanoscale gap, *Nat. Phys.* **16**, 341 (2020).
 - [18] M. R. Bionta, F. Ritzkowski, M. Turchetti, Y. Yang, D. C. Mor, W. P. Putnam, F. X. Kärtner, K. K. Berggren, and P. D. Keathley, On-chip sampling of optical fields with attosecond resolution, *Nat. Photon.* **15**, 456 (2021).
 - [19] Y. Luo, A. Martin-Jimenez, F. Neubrech, N. Liu, and M. Garg, Synthesis and direct sampling of single-cycle light transients by electron tunneling in a nanodevice, *ACS Photonics* **10**, 2866 (2023).
 - [20] V. Gerstner, A. Knoll, W. Pfeiffer, A. Thon, and G. Gerber, Femtosecond laser assisted scanning tunneling microscopy, *J. Appl. Phys.* **88**, 4851 (2000).
 - [21] S. Grafström, Photoassisted scanning tunneling microscopy, *J. Appl. Phys.* **91**, 1717 (2002).
 - [22] M. Merschdorf, W. Pfeiffer, A. Thon, and G. Gerber, Hot electron tunneling in femtosecond laser-assisted scanning tunneling microscopy, *Appl. Phys. Lett.* **81**, 286 (2002).
 - [23] Y. Terada, S. Yoshida, O. Takeuchi, and H. Shigekawa, Real-space imaging of transient carrier dynamics by nanoscale pump-probe microscopy, *Nat. Photon.* **4**, 869 (2010).
 - [24] S. Dey, D. Mirell, A. R. Perez, J. Lee, and V. A. Apkarian, Nonlinear femtosecond laser induced scanning tunneling microscopy, *J. Chem. Phys.* **138**, 154202 (2013).
 - [25] M. Garg and K. Kern, Attosecond coherent manipulation of electrons in tunneling microscopy, *Science* **367**, 411 (2020).
 - [26] T. L. Cocker, D. Peller, P. Yu, J. Repp, and R. Huber, Tracking the ultrafast motion of a single molecule by femtosecond orbital imaging, *Nature* **539**, 263 (2016).
 - [27] S. Kim, T. Schmude, G. Burkard, and A. S. Moskalenko, Quasiclassical theory of non-adiabatic tunneling in nanocontacts induced by phase-controlled ultrashort light pulses, *New J. Phys.* **23**, 083006 (2021).
 - [28] Z. Hu, Y. Kwok, G. Chen, and S. Mukamel, Carrier-envelope-phase modulated currents in scanning tunneling microscopy, *Nano Lett.* **21**, 6569 (2021).
 - [29] L. Bhan, C. Covington, and K. Varga, Signatures of atomic structure in subfemtosecond laser-driven electron dynamics in nanogaps, *Phys. Rev. B* **105**, 085416 (2022).
 - [30] M. Lewenstein, P. Balcou, M. Y. Ivanov, A. L'Huillier, and P. B. Corkum, Theory of high-harmonic generation by low-frequency laser fields, *Phys. Rev. A* **49**, 2117 (1994).
 - [31] D. B. Milošević, G. G. Paulus, D. Bauer, and W. Becker, Above-threshold ionization by few-cycle pulses, *J. Phys. B: At. Mol. Opt. Phys.* **39**, R203 (2006).
 - [32] K. Amini, J. Biegert, F. Calegari, A. Chacón, M. F. Ciappina, A. Dauphin, D. K. Efimov, C. F. de Morisson Faria, K. Giergiel, P. Gniewek, A. S. Landsman, M. Lesiuk, M. Mandrysz, A. S. Maxwell, R. Moszyński, L. Ortmann, J. A. Pérez-Hernández, A. Picón, E. Pisanty, J. Prauzner-Bechcicki, K. Sacha, N. Suárez, A. Zaïr, J. Zakrzewski, and M. Lewenstein, Symphony on strong field approximation, *Rep. Prog. Phys.* **82**, 116001 (2019).
 - [33] P. B. Corkum, Plasma perspective on strong field multiphoton ionization, *Phys. Rev. Lett.* **71**, 1994 (1993).
 - [34] K. C. Kulander, K. J. Schafer, and J. L. Krause, Dynamics of short-pulse excitation, ionization and harmonic conversion, in *Super-Intense Laser-Atom Physics (SILAP) III*, edited by B. Piraux, A. L'Huillier, and K. Rzażewski (Plenum Press (New York), 1993) p. 95.
 - [35] M. Ferray, A. L'Huillier, X. F. Li, L. A. Lompre, G. Mainfray, and C. Manus, Multiple-harmonic conversion of 1064 nm radiation in rare gases, *J. Phys. B: At. Mol. Opt. Phys.* **21**, L31 (1988).
 - [36] G. G. Paulus, W. Nicklich, H. Xu, P. Lambropoulos, and H. Walther, Plateau in above threshold ionization spectra, *Phys. Rev. Lett.* **72**, 2851 (1994).
 - [37] D. N. Fittinghoff, P. R. Bolton, B. Chang, and K. C. Kulander, Observation of nonsequential double ionization of helium with optical tunneling, *Phys. Rev. Lett.* **69**, 2642 (1992).
 - [38] See Supplemental Material at [URL will be inserted by publisher] for complete derivations, supplemental discussions, and supplemental figures, which includes Refs. [39–45].
 - [39] K. Yoshioka, I. Katayama, Y. Minami, M. Kitajima, S. Yoshida, H. Shigekawa, and J. Takeda, Real-space coherent manipulation of electrons in a single tunnel junction by single-cycle terahertz electric fields, *Nat. Photon.* **10**, 762 (2016).
 - [40] V. Jelic, K. Iwaszczuk, P. H. Nguyen, C. Rathje, G. J. Hornig, H. M. Sharum, J. R. Hoffman, M. R. Freeman, and F. A. Hegmann, Ultrafast terahertz control of extreme tunnel currents through single atoms on a silicon surface, *Nat. Phys.* **13**, 591 (2017).
 - [41] Y. Luo and P. Zhang, Ultrafast optical-field-induced photoelectron emission in a vacuum nanoscale gap: An exact analytical formulation, *Appl. Phys. Lett.* **119**, 194101 (2021).
 - [42] O. Smirnova and M. Ivanov, Multielectron high harmonic generation: Simple man on a complex plane, in *Attosecond and XUV Physics* (Wiley-VCH Verlag GmbH und Co. KGaA, 2014) pp. 201–256.
 - [43] O. Pedatzur, G. Orenstein, V. Serbinenko, H. Soifer, B. D. Bruner, A. J. Uzan, D. S. Brambila, A. G. Harvey, L. Torlina, F. Morales, O. Smirnova, and N. Dudovich, Attosecond tunnelling interferometry, *Nat. Phys.* **11**, 815 (2015).
 - [44] C. Ott, M. Schönwald, P. Raith, A. Kaldun, G. Sansone, M. Krüger, P. Hommelhoff, Y. Patil, Y. Zhang, K. Meyer, M. Laux, and T. Pfeifer, Strong-field spectral interferometry using the carrier-envelope phase, *New J. Phys.* **15**, 073031 (2013).
 - [45] P. Hommelhoff, Y. Sortais, A. Aghajani-Talesh, and M. A. Kasevich, Field emission tip as a nanometer source of free electron femtosecond pulses, *Phys. Rev. Lett.* **96**, 077401 (2006).
 - [46] J. Bardeen, Tunnelling from a many-particle point of view, *Phys. Rev. Lett.* **6**, 57 (1961).
 - [47] C. J. Chen, *Introduction to Scanning Tunneling Microscopy* (Oxford University Press, 2021).

- [48] M. Y. Ivanov, M. Spanner, and O. Smirnova, Anatomy of strong field ionization, *J. Mod. Opt.* **52**, 165 (2005).
- [49] S. V. Yalunin, M. Gulde, and C. Ropers, Strong-field photoemission from surfaces: Theoretical approaches, *Phys. Rev. B* **84**, 195426 (2011).
- [50] J. Pitarke, F. Flores, and P. Echenique, Tunneling spectroscopy: surface geometry and interface potential effects, *Surf. Sci.* **234**, 1 (1990).
- [51] G. Wachter, C. Lemell, J. Burgdörfer, M. Schenk, M. Krüger, and P. Hommelhoff, Electron rescattering at metal nanotips induced by ultrashort laser pulses, *Phys. Rev. B* **86**, 035402 (2012).
- [52] L. V. Keldysh, Ionization in the field of a strong electromagnetic wave, *Sov. Phys. JETP* **20**, 1307 (1965).
- [53] M. Garg, A. Martin-Jimenez, Y. Luo, and K. Kern, Ultrafast photon-induced tunneling microscopy, *ACS Nano* **15**, 18071 (2021).
- [54] M. Garg, A. Martin-Jimenez, M. Pizarra, Y. Luo, F. Martín, and K. Kern, Real-space subfemtosecond imaging of quantum electronic coherences in molecules, *Nat. Photon.* **16**, 196 (2022).
- [55] R. Bormann, M. Gulde, A. Weismann, S. V. Yalunin, and C. Ropers, Tip-enhanced strong-field photoemission, *Phys. Rev. Lett.* **105**, 147601 (2010).
- [56] P. Dombi, S. E. Irvine, P. Rácz, M. Lenner, N. Kroó, G. Farkas, A. Mitrofanov, A. Baltuška, T. Fuji, F. Krausz, and A. Y. Elezzabi, Observation of few-cycle, strong-field phenomena in surface plasmon fields, *Optics Expr.* **18**, 24206 (2010).
- [57] M. Krüger, C. Lemell, G. Wachter, J. Burgdörfer, and P. Hommelhoff, Attosecond physics phenomena at nanometric tips, *J. Phys. B: At. Mol. Opt. Phys.* **51**, 172001 (2018).
- [58] P. Dombi, Z. Pápa, J. Vogelsang, S. V. Yalunin, M. Sivilis, G. Herink, S. Schäfer, P. Groß, C. Ropers, and C. Lienau, Strong-field nano-optics, *Rev. Mod. Phys.* **92**, 025003 (2020).
- [59] P. Salières, B. Carré, L. Le Déroff, F. Grasbon, G. G. Paulus, H. Walther, R. Kopold, W. Becker, D. B. Milošević, A. Sanpera, and M. Lewenstein, Feynman's path-integral approach for intense-laser-atom interactions, *Science* **292**, 902 (2001).
- [60] A. M. Zheltikov, Keldysh parameter, photoionization adiabaticity, and the tunneling time, *Phys. Rev. A* **94**, 043412 (2016).
- [61] G. Herink, D. R. Solli, M. Gulde, and C. Ropers, Field-driven photoemission from nanostructures quenches the quiver motion, *Nature* **483**, 190 (2012).
- [62] M. F. Ciappina, J. A. Pérez-Hernández, T. Shaaran, L. Roso, and M. Lewenstein, Electron-momentum distributions and photoelectron spectra of atoms driven by an intense spatially inhomogeneous field, *Phys. Rev. A* **87**, 063833 (2013).
- [63] G. L. Yudin and M. Y. Ivanov, Nonadiabatic tunnel ionization: Looking inside a laser cycle, *Phys. Rev. A* **64**, 013409 (2001).

Strong-Field Theory of Attosecond Tunneling Microscopy – Supplemental Material –

Boyang Ma^{1,2,3} and Michael Krüger^{1,2,3,*}

¹*Department of Physics, Technion—Israel Institute of Technology, Haifa 32000, Israel*

²*Solid State Institute, Technion—Israel Institute of Technology, Haifa 32000, Israel*

³*The Helen Diller Quantum Center, Technion—Israel Institute of Technology, Haifa 32000, Israel*

(Dated: October 1, 2024)

I. INDUCED CURRENTS IN THE LASER-DRIVEN SCANNING TUNNELING MICROSCOPE

A conventional scanning tunneling microscope (STM) consists of a conductive nanotip and a sample separated by a vacuum gap. Within a simple description of the STM using the Schrödinger equation, the metal-vacuum-metal sandwich structure can be described as two potential wells separated by a thin vacuum potential barrier. Therefore, wavefunctions located in the tip and sample can bifurcate into a tunneling wave and a reflected wave separately in these two potential wells after evolution. The continuity equation $(\partial/\partial t)|\Psi|^2 + \nabla \cdot J = 0$ should be satisfied by the evolving wavefunctions in any region and at any time. Integrating it over time and space, we can derive the time-accumulated currents on the boundaries of a specific region and evaluate the probability difference between the final time and initial time in this region:

$$\int_{-\infty}^{+\infty} J_2 dt - \int_{-\infty}^{+\infty} J_1 dt = - \left[\langle \Psi(+\infty) | \chi_{(x_1, x_2)} | \Psi(+\infty) \rangle - \langle \Psi(-\infty) | \chi_{(x_1, x_2)} | \Psi(-\infty) \rangle \right]. \quad (S1)$$

Here we have used $-\infty$ and $+\infty$ to denote the initial time and the final time. We define an operator $\chi_{(x_1, x_2)}$ in order to select values in $x \in (x_1, x_2)$. Inside the vacuum gap, the wavefunctions will return to their initial state after a sufficiently long time. Therefore, we obtain the flux conservation of currents (J_t and J_s) from the tip and the sample, respectively:

$$\int_{-\infty}^{+\infty} J_s dt = \int_{-\infty}^{+\infty} J_t dt. \quad (S2)$$

To obtain the total current, we apply Eq. S1 to the sample region and let $J_\infty = 0$. The wavefunction in the tip (or sample) $|\Psi_t\rangle$ ($|\Psi_s\rangle$) bifurcates into a tunneling wavefunction $|\Psi_{tT}\rangle$ ($|\Psi_{sT}\rangle$) in the sample (tip) and a reflected wavefunction $|\Psi_{tR}\rangle$ ($|\Psi_{sR}\rangle$) in the tip (sample). Since the electrons emitted from the tip and the sample can have a random global phase, we multiply a phase factor $\exp(i\phi)$ to the $|\Psi_s\rangle$. Considering N laser pulses, the average current per pulse is

$$\begin{aligned} \mathcal{J} &= \frac{1}{N} \sum_{n=1}^N \int_{-\infty}^{+\infty} J_s dt \\ &= \frac{1}{N} \sum_{n=1}^N \{ \langle \Psi_{tT} + \Psi_{sR} e^{i\phi(n)} | \Psi_{tT} + \Psi_{sR} e^{i\phi(n)} \rangle - \langle \Psi_s | \Psi_s \rangle \} \\ &= \frac{1}{N} \sum_{n=1}^N \{ \langle \Psi_{tT} + \Psi_{sR} e^{i\phi(n)} | \Psi_{tT} + \Psi_{sR} e^{i\phi(n)} \rangle \\ &\quad - \langle \Psi_{sT} + \Psi_{sR} | e^{-i\phi(n)} U(+\infty, -\infty) U^\dagger(+\infty, -\infty) e^{i\phi(n)} | \Psi_{sT} + \Psi_{sR} \rangle \} \\ &= \frac{1}{N} \sum_{n=1}^N \{ \langle \Psi_{tT} | \Psi_{tT} \rangle - \langle \Psi_{sT} | \Psi_{sT} \rangle + 2\Re(e^{i\phi(n)} \langle \Psi_{tT} | \Psi_{sR} \rangle) \} \\ &= \langle \Psi_{tT} | \Psi_{tT} \rangle - \langle \Psi_{sT} | \Psi_{sT} \rangle \end{aligned} \quad (S3)$$

* Corresponding author: krueger@technion.ac.il

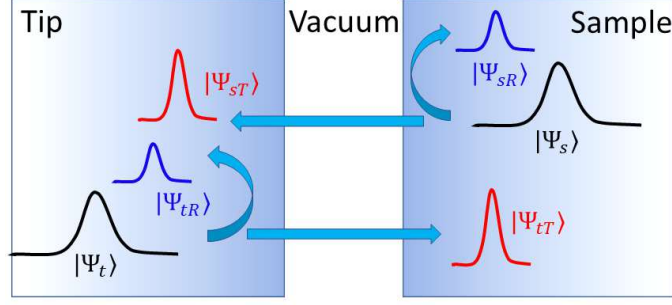


Figure S1. Wavefunctions in the tip and sample bifurcate into the reflected wavefunctions and tunneling wavefunctions separately at the final time.

Equation S3 shows that the contributions to the current are from the tunneling probabilities in the tip and the sample. The other contributions are averaged out.

II. DERIVATION OF THE TUNNELING AMPLITUDE

We define the field-free STM potential with the Fermi energy $E_{F,t}$ and $E_{F,s}$ as well as work functions W_t and W_s for tip and sample [1, 2], respectively:

$$V_0 = \begin{cases} -(E_{F,t} + W_t), & x < 0, \\ V_{\text{imag}}(x) - e(\varphi + U_s)x/d, & 0 \leq x \leq d, \\ -(E_{F,s} + W_s + e\varphi + eU_s), & x > d \end{cases} \quad (\text{S4})$$

where $e = -|e|$ is the charge of the electron, $V_{\text{imag}}(x)$ is the image potential defined in [1], $\varphi = (W_t - W_s)/e$ is the contact potential difference, also known as Volta potential, and U_s is the static bias voltage applied to the STM. The tip boundary is set at $x = 0$ and the sample boundary is at $x = d$. Furthermore, we assume the tip and sample are ideal metals that can screen the laser field perfectly. The interaction V_I under the length gauge is given by

$$V_I(t) = \begin{cases} 0, & x < 0, \\ -e\mathcal{E}(t)x, & 0 \leq x \leq d, \\ -e\mathcal{E}(t)d, & x > d \end{cases} \quad (\text{S5})$$

The total potential with interaction in the Hamiltonian is $V(t) = V_0 + V_I(t)$. In the following, we will use χ_t , χ_{gap} , and χ_s to select wavefunctions in the tip, gap, and sample, respectively. They will be 1 in the labeled regions and 0 outside these regions. The laser-induced tunneling is due to electrons driven across the gap by the laser field. Therefore, based on the Dyson equation, we can expand the evolution operator to the third order,

$$\begin{aligned} U(t, -\infty) &= U_0(t, -\infty) + \left(-\frac{i}{\hbar}\right) \int_{-\infty}^t U(t, t_1) \chi_s V_I(t_1) U_0(t_1, -\infty) dt_1 \\ &+ \left(-\frac{i}{\hbar}\right) \int_{-\infty}^t U_{\text{Is}}(t, t_1) \chi_{\text{gap}} V_I(t_1) U_0(t_1, -\infty) dt_1 \\ &+ \left(-\frac{i}{\hbar}\right)^2 \int_{-\infty}^t \int_{-\infty}^{t_2} U(t, t_2) [\chi_t + \chi_s] [V(t_2) - V_{\text{Is}}(t_2)] \\ &\quad \times U_{\text{Is}}(t_2, t_1) \chi_{\text{gap}} V_I(t_1) U_0(t_1, -\infty) dt_1 dt_2. \end{aligned} \quad (\text{S6})$$

where $U_0(\cdot, \cdot)$ is the evolution operator with the interaction-free potential V_0 . V_{Is} is the interaction with partially static potentials

$$V_{\text{Is}}(t) = \begin{cases} 0, & x < 0, \\ V_{\text{imag}}(x) - ex[\mathcal{E}(t) + (\varphi + U_s)/d], & 0 \leq x \leq d, \\ -e[\mathcal{E}(t)d + \varphi + U_s], & x > d \end{cases} \quad (\text{S7})$$

and $U_{\text{Is}}(\cdot, \cdot)$ is the evolution operator with V_{Is} . The first term of Eq. S6 describes the evolution of the non-perturbed initial wave function. In contrast, the second term selects a perturbed region inside the sample, representing the initial wave function that has finished its tunneling before the laser comes. These two terms are unrelated to the laser-induced tunneling. They can be removed by the relation of Eq. S3.

When these operators work on the wave functions, we obtain the laser-induced tunneling amplitude $M_E(t)$ as

$$\begin{aligned} M_E(t) &= \langle \psi_E(t) | \chi_s U(t, -\infty) | \Psi_0(-\infty) \rangle \\ &= \langle \psi_E(t) | \chi_s | \Psi_{\text{Is}}(t) \rangle + \left(-\frac{i}{\hbar} \right) \int_{-\infty}^t \langle \psi(t_1) | [\chi_t + \chi_s] [V(t_1) - V_{\text{Is}}(t_1)] | \Psi_{\text{Is}}(t_1) \rangle dt_1, \end{aligned} \quad (\text{S8})$$

where $\langle \psi(t_1) | = \langle \psi_E(t) | \chi_s U(t, t_1)$ and $|\Psi_{\text{Is}}(t)\rangle = \left(-\frac{i}{\hbar} \right) \int_{-\infty}^t U_{\text{Is}}(t, t_1) \chi_{\text{gap}} V_{\text{I}}(t_1) \Psi_0(t_1) dt_1$. Ψ_0 is the initial wavefunction and ψ_E is an eigenfunction of the sample with energy E .

Next, we use the following two equations,

$$\langle \psi(t) | (-i\hbar \frac{\partial}{\partial t} - H_0) [\chi_t + \chi_s] = \langle \psi(t) | V(t) [\chi_t + \chi_s] \quad (\text{S9})$$

and

$$[\chi_t + \chi_s] (i\hbar \frac{\partial}{\partial t} - H_0) | \Psi_{\text{Is}}(t) \rangle = [\chi_t + \chi_s] V_{\text{Is}}(t) | \Psi_{\text{Is}}(t) \rangle \quad (\text{S10})$$

and apply them to Eq. S8. In space representation, the integration of the second term of Eq. S8 is executed using partial integration in the following calculation,

$$\begin{aligned} &\left(-\frac{i}{\hbar} \right) \int_{-\infty}^t \langle \psi(t_1) | [\chi_t + \chi_s] [V(t_1) - V_{\text{Is}}(t_1)] | \Psi_{\text{Is}}(t_1) \rangle dt_1 \\ &= \int_{-\infty}^t \int_{-\infty}^{\infty} [\chi_t + \chi_s] \left[\Psi_{\text{Is}}(x, t_1) \left(-\frac{\partial}{\partial t_1} - \frac{i\hbar}{2m} \frac{\partial^2}{\partial x^2} \right) \psi^*(x, t_1) - \psi^*(x, t_1) \left(\frac{\partial}{\partial t_1} - \frac{i\hbar}{2m} \frac{\partial^2}{\partial x^2} \right) \Psi_{\text{Is}}(x, t_1) \right] dx dt_1 \\ &= -\langle \psi(t) | [\chi_t + \chi_s] | \Psi_{\text{Is}}(t) \rangle - \frac{i\hbar}{2m} \int_{-\infty}^t \int_{-\infty}^{\infty} [\chi_t + \chi_s] \frac{\partial}{\partial x} \left[\Psi_{\text{Is}}(x, t_1) \frac{\partial}{\partial x} \psi^*(x, t_1) - \psi^*(x, t_1) \frac{\partial}{\partial x} \Psi_{\text{Is}}(x, t_1) \right] dx dt_1 \\ &= -\langle \psi_E(t) | \chi_s [\chi_t + \chi_s] | \Psi_{\text{Is}}(t) \rangle + \frac{i\hbar}{2m} \int_{-\infty}^t \left[\Psi_{\text{Is}}(x, t_1) \frac{\partial}{\partial x} \psi^*(x, t_1) - \psi^*(x, t_1) \frac{\partial}{\partial x} \Psi_{\text{Is}}(x, t_1) \right] \Big|_{x=0}^{x=d} dt_1 \\ &= -\langle \psi_E(t) | \chi_s | \Psi_{\text{Is}}(t) \rangle + \frac{i\hbar}{2m} \int_{-\infty}^t \left[\Psi_{\text{Is}}(x, t_1) \frac{\partial}{\partial x} \psi^*(x, t_1) - \psi^*(x, t_1) \frac{\partial}{\partial x} \Psi_{\text{Is}}(x, t_1) \right] \Big|_{x=0}^{x=d} dt_1. \end{aligned} \quad (\text{S11})$$

The first term of these results just cancels the first term in Eq. S8, hence the simplified tunneling amplitude at an arbitrary time now reads

$$M_E(t) = \frac{i\hbar}{2m} \int_{-\infty}^t \left[\Psi_{\text{Is}}(x, t_1) \frac{\partial}{\partial x} \psi^*(x, t_1) - \psi^*(x, t_1) \frac{\partial}{\partial x} \Psi_{\text{Is}}(x, t_1) \right] \Big|_{x=0}^{x=d} dt_1. \quad (\text{S12})$$

The notation $[...]_{x=0}^{x=d}$ at the end stands for the subtraction of the term inside the brackets evaluated at $x = 0$ from the term evaluated at $x = d$. For the tunneling from the sample, the amplitude is calculated in the same way but we need to use the opposite sign of the instantaneous laser field [3].

For the accumulated tunneling current, the final measurement time can be set at infinity, when the interaction has been finished. The laser-induced tunneling magnitude is then given by

$$M_E = \frac{i\hbar}{2m} \int_{-\infty}^{\infty} \left[\Psi_{\text{Is}}(x, t_1) \frac{\partial}{\partial x} \psi^*(x, t_1) - \psi^*(x, t_1) \frac{\partial}{\partial x} \Psi_{\text{Is}}(x, t_1) \right] \Big|_{x=0}^{x=d} dt_1, \quad (\text{S13})$$

which has the same form as Bardeen's tunneling theory [4]. Figure S2 shows a comparison of Eq. S13 with the TDSE. The results are exactly identical.

By inserting the completeness operator into the current (Eq. S3), we obtain the relation between tunneling amplitude Eq. S13 and the net current.

$$\begin{aligned} \mathcal{J} &= \langle \Psi_{tT} | \Psi_{tT} \rangle - \langle \Psi_{sT} | \Psi_{sT} \rangle \\ &= \sum_E [\langle \Psi_{tT} | \psi_E(\infty) \rangle \langle \psi_E(\infty) | \Psi_{tT} \rangle - \langle \Psi_{sT} | \psi_E(\infty) \rangle \langle \psi_E(\infty) | \Psi_{sT} \rangle] \\ &= \sum_E (|M_{tE}|^2 - |M_{sE}|^2). \end{aligned} \quad (\text{S14})$$

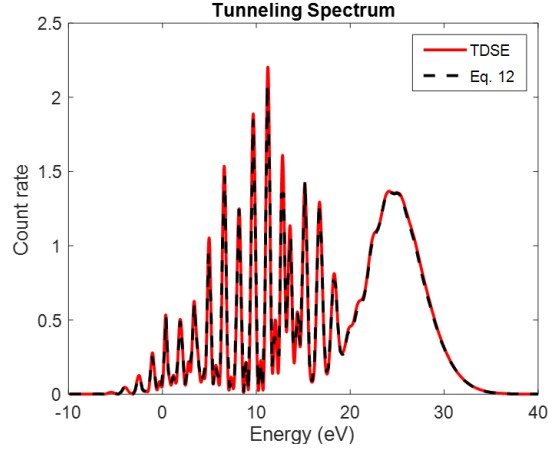


Figure S2. Comparison between TDSE simulation and the numerical calculation of Eq. S13. We use a peak field of $F = 35 \text{ V nm}^{-1}$ for a 6-fs laser pulse at a central wavelength of 830 nm. The width of the STM junction is $d = 1 \text{ nm}$. Tip and sample are chosen to be identical (gold: $E_{F,t} = E_{F,s} = 5 \text{ eV}$, $E_0 = -5 \text{ eV}$, $W_t = W_s = 5 \text{ eV}$). The static bias voltage U_s and the contact potential φ are chosen to be zero.

III. STRONG FIELD APPROXIMATION AND SADDLE POINT EQUATIONS

By using the strong field approximation (SFA) introduced in the main text, the result of Eq. S13 is simplified to

$$M_{E,\text{SFA}} = \frac{i\hbar}{2m} \int_{-\infty}^{\infty} \left[\Psi_V(x, t_1) \frac{\partial}{\partial x} \psi_E^*(x, t_1) - \psi_E^*(x, t_1) \frac{\partial}{\partial x} \Psi_V(x, t_1) \right]_{x=d} dt_1. \quad (\text{S15})$$

where $|\Psi_V(t)\rangle = (-\frac{i}{\hbar}) \int_{-\infty}^t U_V(t, t_1) \chi_{\text{gap}} V_I(t_1) \Psi_0(t_1) dt_1$ is a superposition of the Volkov wave functions, and $U_V(\cdot, \cdot)$ is the Volkov evolution operator. To further simplify and compress this result, we consider an initial wave function at energy E_0 and zero bias voltage. The tip and sample are made from the same material (gold: $E_{F,t} = E_{F,s} = 5 \text{ eV}$, $W_t = W_s = -E_0 = 5 \text{ eV}$).

$$\Psi_0(x) = \begin{cases} e^{ik_1 x} + R e^{-ik_1 x}, & x < 0, \\ B_1 e^{-\frac{1}{\hbar} \alpha x} + B_2 e^{\frac{1}{\hbar} \alpha x}, & 0 \leq x \leq d, \\ T e^{ik_3 x}, & x > d. \end{cases} \quad (\text{S16})$$

where $\alpha = \sqrt{2m|E_0|}$. The Volkov propagator is defined as

$$\langle x_2 | U_V(t_2, t_1) | x_1 \rangle = \sqrt{\frac{m}{2\pi i \hbar (t_2 - t_1)}} e^{\frac{i}{\hbar} (p - eA(t_2)) x_2} e^{-\frac{i}{\hbar} (p - eA(t_1)) x_1} e^{-\frac{i}{\hbar} \frac{\int_{t_1}^{t_2} (p - eA(\tau))^2 d\tau}{2m}}, \quad (\text{S17})$$

where $p \equiv \frac{\int_{t_1}^{t_2} eA(\tau) d\tau + m(x_2 - x_1)}{t_2 - t_1}$. The static field in the gap can be included into the vector potential $A(t) = -\int_{-\infty}^t \mathcal{E}(\tau) d\tau$.

We define two prefactors

$$\begin{aligned} \xi(t_1) \equiv & e\mathcal{E}(t_1) (B_1 \hbar^2 \frac{-1 + [1 + \frac{i}{\hbar} (\tilde{p} - eA(t_1) - i\alpha)d] e^{-\frac{i}{\hbar} (\tilde{p} - eA(t_1) - i\alpha)d}}{(\tilde{p} - eA(t_1) - i\alpha)^2} \\ & + B_2 \hbar^2 \frac{-1 + [1 + \frac{i}{\hbar} (\tilde{p} - eA(t_1) + i\alpha)d] e^{-\frac{i}{\hbar} (\tilde{p} - eA(t_1) + i\alpha)d}}{(\tilde{p} - eA(t_1) + i\alpha)^2}), \end{aligned} \quad (\text{S18})$$

$$\eta(t_2) \equiv (\tilde{p} - eA(t_2) + \sqrt{2m(E - U_s)}) e^{-\frac{i}{\hbar} \sqrt{2m(E - U_s)} d}, \quad (\text{S19})$$

the effective canonical momentum $\tilde{p} = \frac{\int_{t_1}^{t_2} eA(\tau) d\tau + md}{t_2 - t_1}$, and a phase factor based on the semi-classical action

$$S(t_2, t_1) \equiv Et_2 + \frac{\tilde{p}^2}{2m}(t_2 - t_1) - \int_{t_1}^{t_2} \frac{e^2 A^2(\tau)}{2m} d\tau + |E_0|t_1. \quad (\text{S20})$$

With all this in hand, we derive the laser-driven tunneling amplitude $M_{E,\text{SFA}}$ for an initial wavefunction at energy E_0 as

$$M_{E,\text{SFA}} = \int_{-\infty}^{\infty} \int_{-\infty}^{t_2} \sqrt{\frac{i}{8\pi m \hbar^3 (t_2 - t_1)}} \eta(t_2) \xi(t_1) e^{\frac{i}{\hbar} S(t_2, t_1)} dt_1 dt_2. \quad (\text{S21})$$

This temporal integration contains a rapidly oscillating function $e^{\frac{i}{\hbar} S(t_2, t_1)}$ so that it can be analyzed by the saddle point technique. To find the zero points of the phase derivatives $\frac{\partial S(t_2, t_1)}{\partial t_1} \Big|_{t_1=t_{1s}} = \frac{\partial S(t_2, t_1)}{\partial t_2} \Big|_{t_2=t_{2s}} = 0$, we can retrieve the saddle point equations

$$\frac{[\tilde{p}_s - eA(t_{1s})]^2}{2m} = -|E_0|, \quad (\text{S22})$$

$$\int_{t_{1s}}^{t_{2s}} \frac{[\tilde{p}_s - eA(\tau)]}{m} d\tau = d, \quad (\text{S23})$$

$$\frac{[\tilde{p}_s - eA(t_{2s})]^2}{2m} = E. \quad (\text{S24})$$

The subscript (s) indicates that the value is a saddle point.

IV. CLASSICAL TRAJECTORY AND CUTOFF ENERGY

The saddle point equations can be used to formulate semi-classical trajectories of the tunneling electrons and their transport to the sample region. In Newtonian mechanics, the displacement of a classical point-like electron in the laser field is

$$\mathcal{D}(t) = \int_{t_{1s}}^t \frac{[\tilde{p}_s - eA(\tau)]}{m} d\tau. \quad (\text{S25})$$

In our case, the negative initial energy in the saddle point equation causes all the intermediate values to be complex. Therefore, this displacement must be integrated along a contour on the complex plane, in analogy to saddle point equations for HHG, for instance [5].

Figure S3(a) shows our integration contour. It contains three physical processes. The first contour from the initial time t_{1s} to its real part is tunneling, a classically forbidden process. The second contour along the real axis is the classical trajectory inside the junction. The third contour which is from the real axis to the final t_{2s} corresponds to the attenuation during transmission.

Figure S3(b) and (c) show the current burst based on the TDSE and the superposition of possible classical trajectories, respectively. The void space near $x = 0$ in Figure S3(c) is the region where the tunneling process occurs. The trajectories emerge at the tunnel exit.

The cutoff energy is the maximum kinetic energy that a classical electron can gain from the laser field in the process. According to the TDSE simulations shown in Figure S3(b), the central electron burst is around the crest of the laser waveform when the instantaneous field is strongest ($t = 0$). Therefore, we can solve saddle point equations near the crest by using trigonometric functions with central frequency ω of the incident laser. The electric field is described as

$$\mathcal{E}(t) = -F_0 - F \cos(\omega t), \quad (\text{S26})$$

where F_0 is the static field strength from the bias voltage and the contact (Volta) potential, and F is the field strength of the incident laser. The vector potential is given by

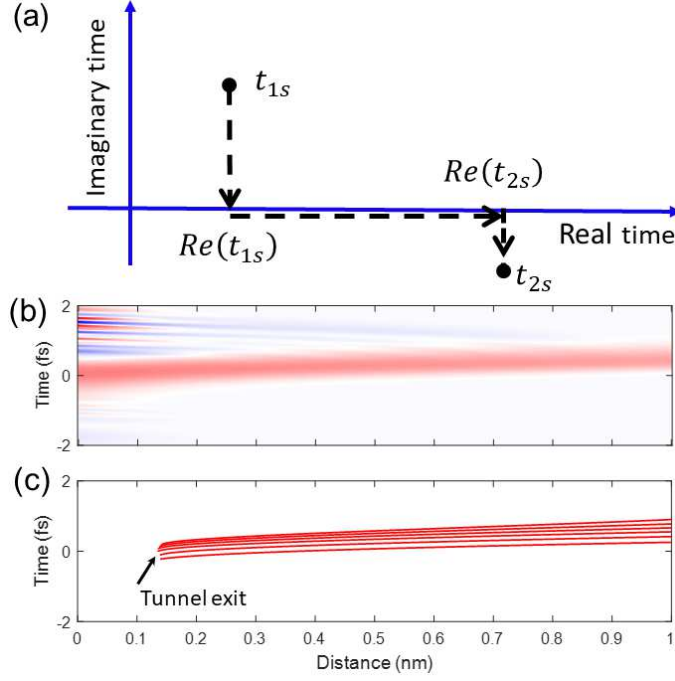


Figure S3. (a) Integration contour on the complex plane for the semi-classical trajectories. (b) and (c) Comparison between the TDSE trajectory and the superposition of several possible classical trajectories. In these simulations, the junction width is $d = 1$ nm, the pulse duration is 3 fs (one cycle), the field strength is 35 V nm^{-1} , and the central wavelength is 830 nm.

$$A(t) = F_0 t + \frac{F}{\omega} \sin(\omega t). \quad (\text{S27})$$

For a lower energetic state, the electron will take more travel time $\tau = t_{2s} - t_{1s}$ to be transported over the junction. In this case, the imaginary part of τ can be approximated with the well-known Keldysh parameter [6, 7],

$$i\omega \Im(\tau) = -\frac{i\omega \sqrt{2m|E_0|}}{|e|(F_0 + F)}. \quad (\text{S28})$$

For a higher energetic state, the freed electron can take a short time to travel across the junction, which causes τ to approach zero. We can use a Taylor expansion to express the duration for this case,

$$\tau = \frac{2md}{\sqrt{2mE} + i\sqrt{2m|E_0|}}. \quad (\text{S29})$$

Figure S4 shows these two approximated solutions for the imaginary part of τ as a function of final energy E in one plot, together with the exact numerical solution. Each of the two solutions agrees well with the exact solution in two separate spectral regions. We note that Eq. S28 has a constant imaginary value and Eq. S29 exhibits a changing imaginary value. In the latter case, the increase of the imaginary part of the travel time leads to a strong attenuation of the tunneling amplitude. Therefore, we define the intersection of these two approximated solutions as the cutoff energy. Equating the imaginary part of Eq. S28 and Eq. S29, we obtain the cutoff energy

$$E_{\text{cutoff}} = |e|(F_0 + F)d - |E_0|. \quad (\text{S30})$$

V. CARRIER-ENVELOPE PHASE MODULATION OF THE TUNNELING CURRENT

For a few-cycle laser pulse, the carrier-envelope phase (CEP) modulation can significantly break the system's symmetry, rectifying the current flow in the junction. The CEP control in the ultrafast STM can be implemented

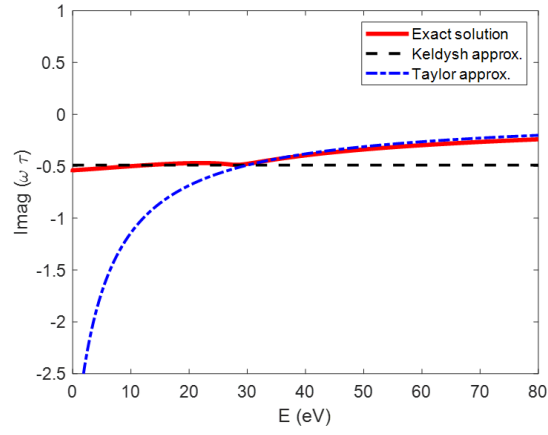


Figure S4. Comparison between two approximated solutions for the imaginary part of the travel time τ with the exact numerical results (red).

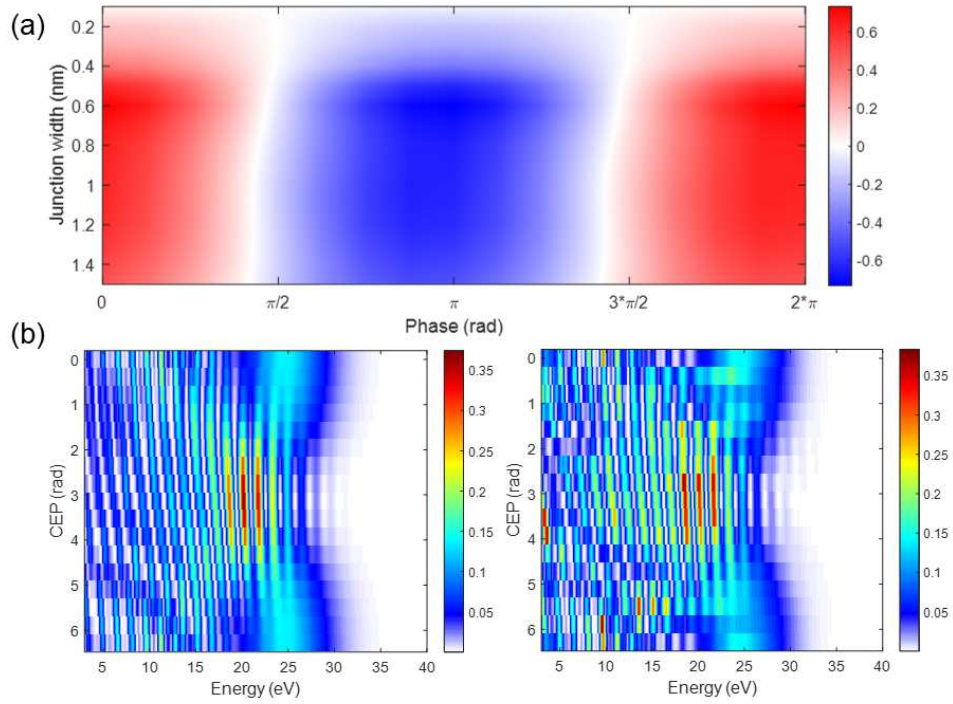


Figure S5. (a) The laser-induced current as a function of CEP and junction width. For a width range from 0.2 nm to 1.5 nm, CEP can efficiently reverse the tunneling currents. In this TDSE simulation, we use 3-fs (one cycle) of field strength $F = 17 \text{ V nm}^{-1}$ laser pulse at 830 nm central wavelength. (b) Energy spectra which are simulated with TDSE (left) and SFA (right) for a 6-fs pulse. The cutoff energies sinusoidally change with respect to the CEP. In these simulations, the field strength is set as 35 V nm^{-1} and the junction width d is 1 nm.

in various conditions such as different junction widths and laser pulse durations. Here, we use the TDSE to test the efficiencies in these conditions. As we have shown in the main text, the CEP effect is only present for sufficiently short laser pulses and is averaged out when the pulse duration becomes large.

The width of the STM junction is another factor that can affect the CEP modulation. In Figure. S5(a), we show that the CEP modulation is quite stable when we retract the tip away from the sample from 0.2 nm to 1.5 nm. This range can basically cover most STM experiments. Even smaller junctions could cause the tip damage. It is also evident that the CEP effect is weak for $d < 0.5 \text{ nm}$, hence larger junction widths are preferred for inducing single attosecond bursts of tunneling electrons.

The CEP modulation can be also interpreted from the energy spectrum based on the SFA. Figure. S5(b) shows

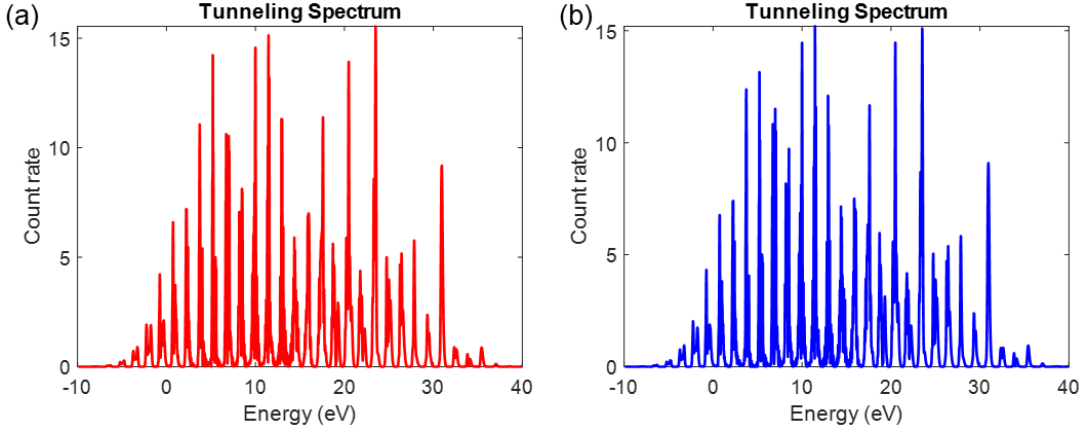


Figure S6. Comparison of the tunneling spectra from the tip to the sample (a) and from the sample to the tip (b). In these TDSE simulations, we use a 50-fs (18 cycles) laser pulse of field strength $F = 35 \text{ V nm}^{-1}$ at 830 nm central wavelength and a junction width d of 1 nm.

a comparison between the TDSE simulation and SFA calculation for a 6-fs laser pulse. The high-energy parts of the spectra are modulated strongly with respect to the CEP. The cutoff energy obtained from the SFA shows linear dependence with field strength F . For short laser pulses, the shift in the CEP changes the effective field strength sinusoidally, leading to these periodical cutoff modulations. Also, interference fringes appear and disappear with CEP at 25 eV near the cutoff, which is a signature of temporal double-slit and single-slit interference, respectively [8, 9]. Furthermore, as what we can see from Fig. 4(b) in the main text, the tunneling current can vanish for long pulses. Figure S6 shows the tunneling spectra from the two sides are almost indistinguishable when the pulse duration is 50 fs (18 cycles).

VI. NUMERICAL CALCULATIONS OF THE TIME-DEPENDENT SCHRÖDINGER EQUATION (TDSE)

In the main text in Fig. 2 and 3, we compare the SFA results with numerical solutions of the TDSE in exactly the same geometry and physical situation. The one-dimensional TDSE is solved using the Crank-Nicolson method, which has been widely used for strong-field physics simulations at nanotips [8, 10–12]. The Hamiltonian in the TDSE is

$$H = -\frac{\hbar^2}{2m} \frac{\partial^2}{\partial x^2} + V_0(x) + V_I(x), \quad (\text{S31})$$

where field-free potential $V_0(x)$ and interaction $V_I(x)$ are defined in Eq. S4 and Eq. S5. In our simulations, we assume that the tip and the sample are made from gold, with a Fermi energy of 5 eV and a work function of 5 eV. The spatial grid and the temporal step size are determined by uncertainty relations

$$\Delta p \cdot \Delta x \geq \frac{\hbar}{2}, \quad (\text{S32})$$

$$\Delta E \cdot \Delta t \sim \hbar. \quad (\text{S33})$$

In our simulations, the maximum expected cutoff energy is 30 eV ($F = 35 \text{ V nm}^{-1}$, $d = 1 \text{ nm}$). Therefore, we set a maximum energy bandwidth $\Delta E = 300 \text{ eV} \gg 30 \text{ eV}$ and apply $\Delta x \rightarrow dx$ and $\Delta t \rightarrow dt$ (here: $\Delta x = 0.01 \text{ nm}$ and $\Delta t = 2.2 \text{ as}$). The incident few-cycle laser electric field has a Gaussian envelope function and its vector potential is given by

$$A(t) = \frac{F}{\omega} e^{-4 \ln 2 (t/\tau)^2} \sin(\omega t + \phi), \quad (\text{S34})$$

where F denotes the peak field strength and ω is the angular frequency. τ and ϕ are the pulse duration (FWHM) and the carrier-envelope phase (CEP), respectively. In our simulations, the laser parameters are $\omega = 2.27 \times 10^{15} \text{ s}^{-1}$ ($\lambda = 830 \text{ nm}$) and $\tau = 6 \text{ fs}$. The calculation time is four times as long as the pulse duration ($-12 \text{ fs} \leq t \leq 12 \text{ fs}$).

In order to avoid undesired reflections of the wave function at the end of the spatial grid, we terminate the grid at positions far away from the tunneling wave functions. A classical point-like electron with a kinetic energy of 30 eV (maximum cutoff energy) can only travel around 40 nm within 12 fs. The termination positions are set at 300 nm, almost 8 times as far away as the fastest electron. The tunneling wave functions are obtained by subtracting the wave function in the sample domain at the initial time from the wave function at the final time. Since the eigenfunctions inside the sample have analytical solutions, we project our simulated tunneling waves directly onto these eigenstates.

-
- [1] K. Yoshioka, I. Katayama, Y. Minami, M. Kitajima, S. Yoshida, H. Shigekawa, and J. Takeda, Real-space coherent manipulation of electrons in a single tunnel junction by single-cycle terahertz electric fields, *Nat. Photon.* **10**, 762 (2016).
 - [2] V. Jelic, K. Iwaszczuk, P. H. Nguyen, C. Rathje, G. J. Hornig, H. M. Sharum, J. R. Hoffman, M. R. Freeman, and F. A. Hegmann, Ultrafast terahertz control of extreme tunnel currents through single atoms on a silicon surface, *Nat. Phys.* **13**, 591 (2017).
 - [3] Y. Luo and P. Zhang, Ultrafast optical-field-induced photoelectron emission in a vacuum nanoscale gap: An exact analytical formulation, *Appl. Phys. Lett.* **119**, 194101 (2021).
 - [4] J. Bardeen, Tunnelling from a many-particle point of view, *Phys. Rev. Lett.* **6**, 57 (1961).
 - [5] O. Smirnova and M. Ivanov, Multielectron high harmonic generation: Simple man on a complex plane, in *Attosecond and XUV Physics* (Wiley-VCH Verlag GmbH und Co. KGaA, 2014) pp. 201–256.
 - [6] L. V. Keldysh, Ionization in the field of a strong electromagnetic wave, *Sov. Phys. JETP* **20**, 1307 (1965).
 - [7] O. Pedatzur, G. Orenstein, V. Serbinenko, H. Soifer, B. D. Bruner, A. J. Uzan, D. S. Brambila, A. G. Harvey, L. Torlina, F. Morales, O. Smirnova, and N. Dudovich, Attosecond tunnelling interferometry, *Nat. Phys.* **11**, 815 (2015).
 - [8] M. Krüger, M. Schenk, and P. Hommelhoff, Attosecond control of electrons emitted from a nanoscale metal tip, *Nature* **475**, 78 (2011).
 - [9] C. Ott, M. Schönwald, P. Raith, A. Kaldun, G. Sansone, M. Krüger, P. Hommelhoff, Y. Patil, Y. Zhang, K. Meyer, M. Laux, and T. Pfeifer, Strong-field spectral interferometry using the carrier-envelope phase, *New J. Phys.* **15**, 073031 (2013).
 - [10] P. Hommelhoff, Y. Sortais, A. Aghajani-Talesh, and M. A. Kasevich, Field emission tip as a nanometer source of free electron femtosecond pulses, *Phys. Rev. Lett.* **96**, 077401 (2006).
 - [11] S. V. Yalunin, M. Gulde, and C. Ropers, Strong-field photoemission from surfaces: Theoretical approaches, *Phys. Rev. B* **84**, 195426 (2011).
 - [12] P. Dienstbier, L. Seiffert, T. Paschen, A. Liehl, A. Leitenstorfer, T. Fennel, and P. Hommelhoff, Tracing attosecond electron emission from a nanometric metal tip, *Nature* **616**, 702 (2023).